The Astrophysical Journal, 951:50 (11pp), 2023 July 1 https://doi.org/10.3847/1538-4357/acd194

Probing the Circumgalactic Medium with Cosmic Microwave Background Polarization Statistical Anisotropy

Anirban Roy[1], Alexander van Engelen[2], Vera Gluscevic[3], and Nicholas Battaglia[1]
[1] Department of Astronomy, Cornell University, Ithaca, NY 14853, USA
[2] School of Earth and Space Exploration, Arizona State University, Tempe, AZ 85287, USA
[3] Department of Physics & Astronomy, University of Southern California, Los Angeles, CA 90007, USA
Received 2022 January 17; revised 2023 March 18; accepted 2023 April 30; published 2023 July 3

Abstract

As cosmic microwave background (CMB) photons traverse the universe, anisotropies can be induced via Thomson scattering (proportional to the electron density; optical depth) and inverse Compton scattering (proportional to the electron pressure; thermal Sunyaev–Zel'dovich effect). Measurements of anisotropy in optical depth τ and Compton y parameters are imprinted by the galaxies and galaxy clusters and are thus sensitive to the thermodynamic properties of the circumgalactic medium and intergalactic medium. We use an analytic halo model to predict the power spectrum of the optical depth ($\tau\tau$), the cross-correlation between the optical depth and the Compton y parameter (τy), and the cross-correlation between the optical depth and galaxy clustering (τg), and compare this model to cosmological simulations. We constrain the optical depths of halos at $z \lesssim 3$ using a technique originally devised to constrain patchy reionization at a higher redshift range. The forecasted signal-to-noise ratio is 2.6, 8.5, and 13, respectively, for a CMB-S4-like experiment and a Vera C. Rubin Observatory–like optical survey. We show that a joint analysis of these probes can constrain the amplitude of the density profiles of halos to 6.5% and the pressure profiles to 13%. These constraints translate to astrophysical parameters, such as the gas mass fraction, f_g, which can be constrained to 5.3% uncertainty at $z \sim 0$. The cross-correlations presented here are complementary to other CMB and galaxy cross-correlations since they do not require spectroscopic galaxy redshifts and are another example of how such correlations are a powerful probe of the astrophysics of galaxy evolution.

Unified Astronomy Thesaurus concepts: Circumgalactic medium (1879); Observational cosmology (1146); Cosmic microwave background radiation (322); Sunyaev-Zeldovich effect (1654); Galaxy cluster counts (583)

1. Introduction

Current-generation cosmic microwave background (CMB) observations by the Planck satellite and various Stage-3 ground-based experiments have mapped the temperature anisotropy with unprecedented precision, saturating the cosmic variance limit on a wide range of angular scales (Aiola et al. 2020; Planck Collaboration et al. 2020; Reichardt et al. 2021). They have, however, only begun to tap the information encoded within the polarization and lensing anisotropy, leaving much to be accomplished by future experiments. The next-generation ground-based observatories, such as Simons Observatory[4] (Ade et al. 2019), CMB-S4[5] (Abazajian et al. 2019), and SPT-3G[6] (Sobrin et al. 2022), are envisioned to realize a dramatic leap forward in terms of polarization and lensing anisotropy measurements on all angular scales, optimizing the science goals tied to the effects on the CMB power-spectra damping tail: neutrino mass measurements, searches for light relic particles, dark matter, etc. The discovery potential of high-resolution polarization measurements, however, goes beyond the damping tail science. In particular, many physical effects produce non-Gaussian footprints in CMB maps, which can be sought with higher-order statistical anisotropy estimators. In this work, we focus on non-Gaussian signatures of secondary anisotropy imprinted by the inhomogeneous distribution of free electrons in halos at $z \lesssim 3$.

The gas present within the virial radii of galaxies and outside their disks is known as the circumgalactic medium (CGM). The CGM connects the interstellar medium to the intergalactic medium and is affected by the physics of the radiative process of galactic winds, active galactic nuclei (AGN), and supernovae feedback (Werk et al. 2014; Nielsen et al. 2015; Tumlinson et al. 2017). These processes change the pressure and density profile of galaxies, and hence, the detection of thermal Sunyaev–Zel'dovich (tSZ) from the CGM is a potential probe to aid in understanding the thermodynamics of halos. Thus, CMB observations can provide a new window into studying the CGM. Several cross-correlation studies, such as tSZ galaxy clustering and tSZ CMB lensing, are also useful to measure the pressure of gas and their evolution in host halos (Hill & Spergel 2014; Battaglia et al. 2015; Hurier et al. 2015; Hojjati et al. 2017; Koukoufilippas et al. 2020; Pandey et al. 2020; Amodeo et al. 2021; Pandey et al. 2022; Yan et al. 2021). The tSZ galaxy clustering cross-correlation has been extensively studied in various aspects to measure the gas mass fraction, the gas temperature, and their evolution (Greco et al. 2015; Singh et al. 2016; Amodeo et al. 2021; Meinke et al. 2021; Moser et al. 2021). Furthermore, the measurements of the kinetic Sunyaev–Zel'dovich (kSZ) effect can provide constraints on the density profiles of gas in halos, and the joint analysis of kSZ and tSZ measurements can break the degeneracies between the parameters. In addition,

[4] https://simonsobservatory.org/
[5] https://cmb-s4.org/
[6] https://pole.uchicago.edu/

cross-correlations with spectroscopic galaxy samples can help us to measure the temperature profile of the halos (Amodeo et al. 2021).

The spatial distribution of free electrons in the universe is inhomogeneous, and the largest contribution to the statistical variance of these fluctuations is generated during the epoch of reionization since the reionization process is highly non-Gaussian in nature. The small-scale temperature and polarization anisotropies in the CMB are suppressed by a factor of $e^{-\tau(\hat{\boldsymbol{n}})}$ due to the effects of "patchy screening," where $\tau(\hat{\boldsymbol{n}})$ is the direction-dependent optical depth (Dvorkin & Smith 2009; Gluscevic et al. 2013). This can be probed by the reconstruction of the optical depth field (Dvorkin & Smith 2009; Gluscevic et al. 2013; Namikawa 2018; Roy et al. 2018; Guzman & Meyers 2021; Roy et al. 2021). Similar to but smaller than the reionization process, galaxies and galaxy clusters at low redshift contribute to these optical depth fluctuations and provide a probe of the distribution of free electrons inside such halos. Although the imprints of halos and the reionization process in the CMB are related to different physical phenomena, their common trait is a qualitatively similar statistical anisotropy signature in CMB maps that requires the same quadratic-estimator techniques to uncover them. Even though the estimators for the reconstruction of optical depth fluctuations (Dvorkin & Smith 2009) were first developed to study the reionization process, we adopt them here to perform a statistical study of the CGM in the low-redshift universe.

Quadratic estimators for reconstructing lensing potential have been widely used to map the matter distribution in the universe (Aghanim et al. 2018), and an attempt to probe the electron density fluctuations was made by implementing a quadratic optical depth estimator to the Planck data (Namikawa 2018). As secondary anisotropies due to the fluctuations in electron density are subdominant to the lensing signal, neglecting the higher-order corrections in lensing and optical depth can bias the reconstruction noise of an estimator. A bispectrum approach was adopted to extract information about the CMB lensing and optical depth simultaneously (Feng & Holder 2019). Their forecast shows the cross-correlation between the reconstructed optical depth and lensing can be detected with a few σ by upcoming CMB experiments. Furthermore, the forecasted detectability of the cross-correlation between the optical depth reconstructed for a CMB-S4-like experiment and the galaxy number count for a Vera C. Rubin Observatory (VRO)–like experiment is at the order of $\sim 8\sigma$ (Feng & Holder 2018).

The measurements of density profiles are particularly important to break the degeneracy between optical depth and peculiar radial velocity in kSZ measurements (e.g., Alonso et al. 2016; Madhavacheril et al. 2019). Other kSZ estimators, such as the projected fields estimator (Ferraro et al. 2016; Hill et al. 2016; Kusiak et al. 2021), the tomographic kSZ estimator (Shao & Fang 2016), and the pairwise kSZ estimator (e.g., De Bernardis et al. 2017; Calafut et al. 2021; Vavagiakis et al. 2021), can further provide the integral constraints' optical depth of halos (the baryon abundance). Though the statistical properties of the optical depth of halos can be inferred only from such kSZ measurements, these cross-correlation techniques reduce various systematic effects.

In this paper, we propose a set of independent probes, such as the cross-correlation between the optical depth and galaxy clustering, and the cross-correlation between the optical depth and the Compton y parameter, to understand the gas physics in the CGM. We thus present sensitivity forecasts for a CMB-S4-like experiment for each of these physical effects and explore survey strategies that maximize the quality of their measurement. We show how future measurements of these signals can constrain the astrophysical parameters of the CGM. Thus, we illustrate the broad range of CGM information available from careful statistical anisotropy measurements with next-generation CMB observations.

This paper is organized as follows. In Section 2, we describe the halo model approach for the calculation of several autopower spectra of optical depth, galaxy overdensity, Compton y, and the cross-power spectrum between them. We compare our model to simulations in Section 3. In Section 4, we describe the noise model for the optical depth estimator, tSZ measurements, and galaxy clustering. We present the key results of our paper in Section 5, and then we present the constraints on astrophysical parameters in Section 6. We finally draw our conclusions in Section 7. Throughout this work, we assume the best-fit ΛCDM cosmological parameters derived from Planck TT, TE, and EE+lowE+lensing signals (Planck Collaboration et al. 2020).

2. Halo Model

In this section, we review and summarize the basic formalism of the halo-model approach to calculate the auto- and cross-power spectra of different observables, such as tSZ, optical depth, and galaxy fields.

2.1. Optical Depth

The integrated electron density along the line of sight is referred to as the optical depth. As the underlying density field is perturbed, it introduces spatial fluctuations in the electron distribution. This leads to the direction dependence of the optical depth, which can be written as

$$\tau(\hat{\boldsymbol{n}}) = \sigma_{\rm T} \int a\, n_{\rm e}(\hat{\boldsymbol{n}}, \chi) d\chi. \tag{1}$$

Here, $n_{\rm e}(\hat{\boldsymbol{n}}, \chi)$ is the electron density along the direction $\hat{\boldsymbol{n}}$ at a comoving distance χ, $\sigma_{\rm T}$ is the Thomson scattering cross section, and a is the scale factor of the universe. The CMB temperature and polarization anisotropy are damped as

$$\Delta T(\hat{\boldsymbol{n}}) = \Delta\tilde{T}(\hat{\boldsymbol{n}}) e^{-\tau(\hat{\boldsymbol{n}})} \tag{2}$$

$$\Delta(Q \pm iU)(\hat{\boldsymbol{n}}) = \Delta(\tilde{Q} \pm i\tilde{U})(\hat{\boldsymbol{n}}) e^{-\tau(\hat{\boldsymbol{n}})}, \tag{3}$$

where $\tilde{T}$ is the temperature and $\tilde{Q}$ and $\tilde{U}$ are the Stokes parameters of CMB polarization at the last scattering surface.

The perturbation on the free electron density $\Delta n_{\rm e}(\hat{\boldsymbol{n}}, \chi)$ introduces the perturbation $\Delta\tau(\hat{\boldsymbol{n}})$ on the sky-averaged optical depth $\bar{\tau}$ as

$$\tau(\hat{\boldsymbol{n}}) = \bar{\tau} + \Delta\tau(\hat{\boldsymbol{n}}). \tag{4}$$

We now proceed to relate the optical depth to the distribution of electrons within halos. To model the electron density within halos, we adopt the fitting formula derived from cosmological simulations for the gas density from Battaglia (2016) as

$$\rho_{\rm fit}(x) = \rho_0 (x/x_c)^{\gamma} [1 + (x/x_c)^{\alpha}]^{-\left(\frac{\beta_\rho + \gamma}{\alpha}\right)}, \tag{5}$$

Table 1
The Parameters Fitted for the Density Profile of Halos with AGN Feedback (Battaglia 2016)

Parameter	A	α_m	α_z
ρ_0	4×10^3	0.29	−0.66
α	0.88	−0.03	0.19
β_ρ	3.83	0.04	−0.025

where $x = r/r_s$, ρ_0 is the amplitude of the density profile, α is the intermediate slope, and β_ρ is the power-law index. Then, the average stacked profile of the gas density becomes $\rho_{3D} = f_b \rho_{\rm fit} \rho_{\rm crit}(z)$, where f_b is the baryon fraction of the universe and $\Omega_{\rm b}/\Omega_{\rm M}$ and $\rho_{\rm crit}$ represents the critical density of the universe. Throughout this work, we keep fixed $\gamma = -0.2$ (Battaglia et al. 2012). The dependence of the parameters ρ_0, α, and β_ρ on the redshift and mass of the halo is fitted with a generic form of equation as

$$X = A_X \left(\frac{M_{200}}{10^{14}\, M_\odot} \right)^{\alpha_{m,X}} (1+z)^{\alpha_{z,X}}. \quad (6)$$

In the above equation, index X refers to the parameters of our choice related to density profiles, ρ_0, α, and β_ρ. A_X is the amplitude of the parameter and $\alpha_{m,X}$ and $\alpha_{z,X}$ are the power-law indices for the mass and redshift scaling, respectively. The values of such fitted parameters are given in Table 1.

Now, the Fourier transform of τ under the Limber approximation becomes (Komatsu & Kitayama 1999; Hill & Pajer 2013)

$$K_\ell^\tau(M, z) = \frac{4\pi r_s \sigma_T}{\ell_s^2} \int dx \frac{\sin(\ell x/\ell_s)}{\ell x/\ell_s} \rho_{\rm 3D}(x, M, z) x^2, \quad (7)$$

where $K_\ell^\tau(M, z)$ is the kernel of the anisotropies of τ related to the density profiles of a halo and $\ell_{\rm s}$ is the multipole moment corresponding to the characteristic scale radius r_s, of the $\rho_{\rm 3D}$ profile. The effective bias of a field is related to the bias of a dark matter halo. The effective bias of the optical depth profile of such a halo can be written as

$$b_\ell^\tau(M, z) = \int_{M_{\rm min}}^{M_{\rm max}} dM \frac{dn(M, z)}{dM} K_\ell^\tau(M, z) b(M, z), \quad (8)$$

where $b(M, z)$ is the halo bias and $dn(M, z)/dM$ is the halo mass function. We use the Tinker halo mass function throughout this work (Tinker et al. 2008).

2.2. Compton y Parameter

The CMB photons get scattered off the hot electron gas present in the halos, which causes additional anisotropies in the CMB temperature (Sunyaev & Zeldovich 1970, 1972). The temperature fluctuation due to the tSZ effect can be expressed as

$$\frac{\Delta T_{\rm tSZ}(\nu, \hat{\boldsymbol{n}})}{T_{\rm CMB}} = g(\nu) y(\hat{\boldsymbol{n}}). \quad (9)$$

In the above equation, $T_{\rm CMB}$ is the sky-averaged temperature and $\Delta T_{\rm tSZ}(\nu)$ is the change of temperature with respect to $T_{\rm CMB}$ at frequency ν. The term $g(\nu)$ describes how the temperature fluctuation due to the tSZ effect changes with frequency. In the nonrelativistic limit, $g(\nu) = x \coth(x/2) - 4$, where $x = h\nu/k_{\rm B}T_{\rm e}$, where $T_{\rm e}$ is the temperature of the electron gas, h is the Planck constant, and $K_{\rm B}$ is the Boltzmann constant. We neglect the relativistic corrections to the spectral shape of the tSZ signal (Nozawa et al. 2006; Chluba et al. 2012).

Table 2
The Parameters Fitted for the Pressure Profile of Halos (Battaglia et al. 2012)

Parameter	A	α_m	α_z
P_0	18.1	0.154	−0.758
x_c	0.497	−0.00865	0.731
β_P	4.35	0.0393	0.415

The Compton y parameter in the direction $\hat{\boldsymbol{n}}$ is given by

$$y(\hat{\boldsymbol{n}}) = \frac{\sigma_{\rm T}}{m_{\rm e} c^2} \int P_{\rm e}(\hat{\boldsymbol{n}}, \chi) d\chi. \quad (10)$$

Here, c is the speed of light in free space and $m_{\rm e}$ is the mass of an electron. $P_{\rm e}(\hat{\boldsymbol{n}}, \chi)$ is the pressure along the direction $\hat{\boldsymbol{n}}$ at a distance χ. For an isothermal medium, the Compton y parameter is proportional to the optical depth of that medium.

To calculate the y parameter, we use the analytic pressure profiles described in Battaglia et al. (2012) that use a GNFW profile (Zhao 1996) to model the pressure. If r is the radius of a halo and r_s is the characteristic scale of such a halo, then the pressure fitted to the generalized Navarro–Frenk–White (NFW) profile is

$$P_{\rm e}(x) = P_0 (x/x_c)^\gamma [1 + (x/x_c)^\alpha]^{-\beta_{\rm P}}. \quad (11)$$

Here, P_0 is the amplitude of pressure, x_c is the fractional core scale radius, and β_P is the power-law index. α and γ are two free parameters of the model. In Equation (6), index X refers to the parameters of our choice related to pressure profiles, P_0, x_c, and β_P. The best-fit values of these parameters are given in Table 2.

Now, the Fourier transform of the y parameter under the Limber approximation becomes (Komatsu & Kitayama 1999; Hill & Pajer 2013)

$$K_\ell^y(M, z) = \frac{4\pi r_s}{\ell_s^2} \int dx \frac{\sin(\ell x/\ell_s)}{\ell x/\ell_s} y(x, M, z) x^2. \quad (12)$$

The effective bias of the y parameter is given by (Pandey et al. 2020)

$$b_\ell^y(M, z) = \int_{M_{\rm min}}^{M_{\rm max}} dM \frac{dn(M, z)}{dM} K_\ell^y(M, z) b(M, z). \quad (13)$$

2.3. Galaxy Overdensity

We model the distributions of galaxies inside dark matter halos using the halo occupation distribution (HOD) model. The mean occupation functions of the central and satellite galaxies in a halo of mass M_h are given by (Zheng et al. 2005)

$$\langle N_{\rm cen}(M_h) \rangle = \frac{1}{2} \left[1 + {\rm erf} \left(\frac{\log M_{\rm h} - \log M_{\rm th}}{\sigma_{\rm logM}} \right) \right], \quad (14)$$

and

$$\langle N_{\rm sat}(M_h) \rangle = \left(\frac{M_{\rm h} - M_{\rm cut}}{M_1} \right)^{\alpha_{\rm g}}. \quad (15)$$

Here, $\langle N_{\rm cen}(M_h)\rangle$ and $\langle N_{\rm sat}(M_h)\rangle$ are the average number density of central and satellite galaxies. $M_{\rm th}$ is the threshold halo mass to host a central galaxy, $M_{\rm cut}$ is the minimum mass for hosting satellite galaxies, $\sigma_{\rm logM}$ is the width of the transition of the step-like error function, $\alpha_{\rm g}$ is the power-law exponent, and M_1 is the mass normalization factor. The value of HOD-model parameters are given as $\log M_{\rm th} = 12.712$, $\sigma_{\rm logM} = 0.287$, $\log M_{\rm cut} = 12.95$, $\log M_1 = 13.62$, and $\alpha = 0.98$ (Zheng et al. 2005).

The Fourier transform of the distribution of satellite galaxies is given by (e.g., Scoccimarro et al. 2001; Pandey et al. 2020)

$$K_\ell^g = \frac{W_{\rm g}(z)}{\chi^2 \bar{n}_{\rm g}(z)} \times \sqrt{2N_{\rm cen}N_{\rm sat}u_{\rm sat} + N_{\rm cen}^2 N_{\rm sat}^2 u_{\rm sat}^2}\,, \quad (16)$$

where $\bar{n}_{\rm g}(z)$ is the mean galaxy number density and $W_{\rm g}(z)$ is the normalized redshift distribution of galaxies that can be expressed as $\frac{c}{H(z)}\frac{dn_{\rm g}}{dz}$. We assume that the distribution of satellite galaxies follows the underlying dark matter over-density field. The term $u_{\rm sat}$, for the truncated NFW profile, is given by (Navarro et al. 1996)

$$u_{\rm sat} = \frac{\delta_c \rho(z)}{x(1+x)^2}, \quad (17)$$

where $\rho(z)$ is the mean density of the universe and δ_c is the characteristic overdensity of halos.

Putting everything together, the effective bias of the galaxies becomes

$$b_\ell^{\rm g}(M,z) = \frac{W_{\rm g}(z)}{\chi^2 \bar{n}_{\rm g}(z)} \int_{M_{\rm min}}^{M_{\rm max}} dM \frac{dn(M,z)}{dM} \times N_{\rm cen}(M)(1 + N_{\rm sat}(M)) u_{\rm sat} b(M,z). \quad (18)$$

2.4. Power Spectrum

The 1-halo contribution to the power spectra can be expressed within the mass range, $M_{\rm min}$ to $M_{\rm max}$, and the redshift range between $z_{\rm min}$ and $z_{\rm max}$ as (Komatsu & Kitayama 1999; Cooray & Sheth 2002)

$$C_\ell^{\rm XY\,(1-halo)} = \int_{z_{\rm min}}^{z_{\rm max}} dz \frac{d^2V}{d\Omega dz} \int_{M_{\rm min}}^{M_{\rm max}} dM \frac{dn(M,z)}{dM} K_\ell^X K_\ell^Y. \quad (19)$$

Here, K_ℓ^X and K_ℓ^Y are the Fourier transform of the kernel of the X and Y observables, respectively. dV is the comoving volume element at $\chi(z)$.

The 2-halo term can be written as (Komatsu & Kitayama 1999; Cooray & Sheth 2002)

$$C_\ell^{\rm XY\,(2-halo)} = \int_{z_{\rm min}}^{z_{\rm max}} dz \frac{d^2V}{d\Omega dz} b_\ell^X(M,z) b_\ell^Y(M,z) \times P_{\rm lin}(k = \ell/\chi, k), \quad (20)$$

where $P_{\rm lin}$ is the matter power spectrum that we calculated using CAMB[7] in the linear regime (Lewis et al. 2000). The cross-power spectrum is the sum of 1-halo and 2-halo terms:

$$C_\ell^{\rm XY} = C_\ell^{\rm XY\,(1-halo)} + C_\ell^{\rm XY\,(2-halo)}. \quad (21)$$

Using Equations (19), (20), and (21), we calculate the autopower spectrum by setting $X = Y$.

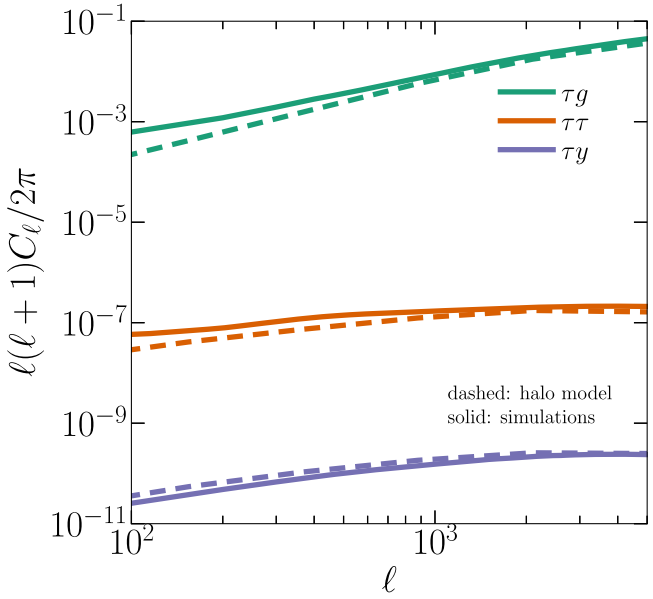

Figure 1. The agreement between the power spectra of τg, τy, and $\tau\tau$ calculated from the hydrodynamic simulations and analytic halo model. We fix $M_{\rm min} = 3 \times 10^{13}\,M_\odot$, $z_{\rm min} = 0$, and $z_{\rm max} = 5$. This validity check ensures we use the halo model calculations reliably for constraining astrophysical parameters of gas thermodynamics in halos.

3. Comparison with Simulations

We validate our results from the analytic halo model against existing cosmological hydrodynamic simulations. These simulations were performed using a modified version of the smoothed particle hydrodynamics code, GADGET-2 (Springel 2005). Included in these simulations were subgrid models for AGN feedback (for more details see Battaglia et al. 2010), radiative cooling, star formation, galactic winds, supernova feedback (for more details see Springel & Hernquist 2003), and cosmic-ray physics (for more details see Pfrommer et al. 2006; Enßlin et al. 2007; Jubelgas et al. 2008). The box sizes for these simulations were 165 Mpc h^{-1}, with a resolution of 256^3 gas and dark matter (DM) particles. This yields mass resolutions of $M_{\rm gas} = 3.2 \times 10^9 M_\odot h^{-1}$ and $M_{\rm DM} = 1.54 \times 10^{10} M_\odot h^{-1}$. Thus, these simulations can resolve more than 1000 particles in halos with masses of $M > 3 \times 10^{13}\,M_\odot$. The cosmological parameters used for these simulations were $\Omega_M = \Omega_{\rm DM} + \Omega_{\rm b} = 0.25$, $\Omega_{\rm b} = 0.043$, $\Omega_\Lambda = 0.75$, $H_0 = 100\,h\,{\rm km\,s^{-1}\,Mpc^{-1}}$, $h = 0.72$, $n_{\rm s} = 0.96$, and $\sigma_8 = 0.8$. These parameters differ from those used in the halo model, but not at the level to cause substantial differences larger than what is currently shown in Figure 1.

We compare the amplitude of $C_\ell^{\tau g}$, $C_\ell^{\tau y}$, and $C_\ell^{\tau\tau}$ estimated from the halo model against the hydrodynamic simulations. The halo-model approach is computationally efficient, and hence, if our results from the halo model are consistent with the results from simulations, we can calibrate our model to study the CGM. In addition, we have more freedom to select the different combinations of astrophysical parameters that we can constrain with future data sets.

[7] https://camb.info

In Figure 1, we show a comparison between the power spectrum estimated from the halo-model approach and hydrodynamic simulations. In doing so, we fixed the minimum halo mass to $3 \times 10^{13} M_{\odot}$ so that it matches with the mass resolution of the simulations. All power spectra agree very well at small scales, $\ell > 1000$. We compare the results from the halo-model approach to the simulations to check if the results are consistent when we fix the exact mass resolution for both cases. As the results agree well on the scales of our interest, we use the halo-model prescriptions for low-mass halos that will be probed by VRO-like experiments. Hence, this consistency check allows us to study the detectability of this signal by changing the different values of $M_{\rm min}$. We then use only the halo model to forecast the parameter constraints on the CGM properties in Section 6.

4. Noise Model

In this section, we review the reconstruction method for optical depth fluctuations and the sources of noise for the measurement of the galaxy and tSZ power spectrum.

4.1. τ Reconstruction Noise

Future CMB experiments promise to reach high-resolution and low-noise measurements of polarization anisotropies, and it increases our ability to measure the $C_\ell^{\tau\tau}$ by applying a reconstruction method (Roy et al. 2018; Namikawa et al. 2021). The fluctuations in the optical depth introduce correlations between different Fourier modes. We can generalize the mode coupling of CMB temperature and polarization as (Dvorkin & Smith 2009)

$$\langle a^{X1}_{\ell_1 m_1} a^{X2}_{\ell_2 m_2} \rangle = \sum_{\ell m} \Gamma^{X_1 X_2}_{\ell_1 \ell_2 \ell} \begin{pmatrix} \ell_1 & \ell_2 & \ell \\ m_1 & m_2 & m \end{pmatrix} (\Delta\tau)^*_{\ell m}, \tag{22}$$

where X_1 and X_2 are any combinations of T, E, and B, and $\ell = \ell_1 + \ell_2$ and $\Gamma^{X_1 X_2}_{\ell_1 \ell_2 \ell}$ is the coupling factors that correlate ℓ_1 and ℓ_2. To minimize the noise of the estimator, we only consider the EB quadratic estimator as it provides the highest signal-to-noise ratio (S/N; Gluscevic et al. 2013). The coupling factor for the EB estimator can be written in terms of Wigner 3-j symbols as

$$\Gamma^{EB}_{\ell_1 \ell_2 \ell} = \frac{C^{EE}_{\ell_1}}{2i} \sqrt{\frac{(2\ell_1+1)(2\ell_2+1)(2\ell+1)}{4\pi}} \times \left[\begin{pmatrix} \ell_1 & \ell_2 & \ell \\ -2 & 2 & 0 \end{pmatrix} - \begin{pmatrix} \ell_1 & \ell_2 & \ell \\ 2 & -2 & 0 \end{pmatrix} \right], \tag{23}$$

where C_ℓ^{EE} is the power spectrum of the E-mode polarization field. The noise for τ reconstruction depends on the sensitivity and resolution of the CMB experiment. The reconstructed τ field is given by (Dvorkin & Smith 2009)

$$\tilde{\tau}^*_{\ell m} = N^{\tau\tau}_\ell \sum_{\ell_1 \ell_2} \sum_{m_1 m_2} \Gamma^{EB^*}_{\ell_1 \ell_2 \ell} \begin{pmatrix} \ell_1 & \ell_2 & \ell \\ m_1 & m_2 & m \end{pmatrix} \times \frac{a^{E^*}_{\ell_1 m_1} a^{B^*}_{\ell_2 m_2}}{(C^{EE}_{\ell_1} + N^{EE}_{\ell_1})(C^{BB}_{\ell_2} + N^{BB}_{\ell_2})}, \tag{24}$$

where C_ℓ^{EE} and C_ℓ^{BB} are the power spectra of the E and B modes. We note that here we only consider the "screening" contribution arising from an inhomogeneous optical depth and do not include the extra information from new polarizations generated from scattering from incident quadrupoles (e.g., Dvorkin et al. 2009). For C_ℓ^{BB}, our forecast includes iterated delensing (Smith et al. 2012), which we assume does not get modulated by the B modes induced by τ fluctuations. N_ℓ^{EE} and N_ℓ^{BB} are instrumental noise power spectra for E- and B-mode signals, respectively. The instrumental noise power spectra are given by (Knox 1995)

$$N_\ell^{EE} = N_\ell^{BB} = \Delta_{\rm P}^2 \exp\left[\frac{\ell(\ell+1)\theta_{\rm f}^2}{8 \ln 2} \right]. \tag{25}$$

In the above equation, $\Delta_{\rm P}$ is the polarization sensitivity of a CMB experiment, which is $\sqrt{2}$ times larger than the sensitivity in temperature, and $\Delta_{\rm T}$ and $\theta_{\rm f}$ are the FWHM of the beam size.

Finally, the reconstruction noise $N_\ell^{\tau\tau}$ is given by (Dvorkin & Smith 2009)

$$N_\ell^{\tau\tau} = \left[\frac{1}{2\ell+1} \sum_{\ell_1 \ell_1} \frac{|\Gamma^{EB^*}_{\ell_1 \ell_2 \ell}|^2}{(C^{EE}_{\ell_1} + N^{EE}_{\ell_1})(C^{BB}_{\ell_2} + N^{BB}_{\ell_2})} \right]^{-1}. \tag{26}$$

We calculate the τ reconstruction noise for CMB-S4-like experiments with 1 μK arcmin sensitivity in temperature and $1'$ beam size (Abazajian et al. 2019). Unless mentioned, we use $l_{\rm min} = 30$ and $l_{\rm max} = 5000$ throughout this work because a CMB-S4-like experiment will make observations at these scales.

This process is analogous to the reconstruction method of the lensing potential from the CMB. In practice, both lensing and patchy reionization signals are present in the CMB data, and if we apply only the τ estimator, there will be leakage from the lensing field to the τ field (Dvorkin & Smith 2009; Su et al. 2011). This problem can be dealt with by applying a "bias-hardened" τ estimator that is insensitive to lensing at leading order fields (Namikawa et al. 2013, 2021). In order to determine the impact of bias hardening the τ estimator from lensing, we computed the τ reconstruction noise $N_\ell^{\tau\tau}$ for bias-hardened estimators, for both TT and EB. We found that for the TT estimator, the bias hardening can increase the lensing reconstruction noise $N_\ell^{\tau\tau}$ by factors of 2–3 across all relevant ℓ values for the S4-like experiment. However, for the EB estimator, bias hardening for lensing has a negligible effect on $N_\ell^{\tau\tau}$ for all but the very highest ℓ values, namely $\ell \gtrsim 4500$. Thus, we do not use the bias-hardened EB noise curves in this work.

In Figure 3, we show the amplitude and shape of $N_\ell^{\tau\tau}$ that depend on the experiment. We vary the sensitivity of an experiment while keeping the beam size fixed to $1'$. The reconstruction noise power spectrum decreases by a factor of 56 if the sensitivity of a CMB experiment is decreased from 9 μK arcmin to 1 μK arcmin at $\ell = 1000$. The power spectra of optical depth from reionization and halos at $\ell = 1000$ are roughly 3 and 4 orders of magnitude smaller than the noise with $\Delta_T = 1$ μK arcmin.

4.2. Noise for tSZ Measurements

We calculate the noise contribution in the yy autopower spectrum, N_ℓ^{yy}, by applying a constrained internal linear combination (cILC) algorithm. The cILC method depends on the assumption that the signal of our interest, tSZ, does not depend on the other signals and noise components and nulls a given contamination signal (Eriksen et al. 2004; Remazeilles et al. 2011).

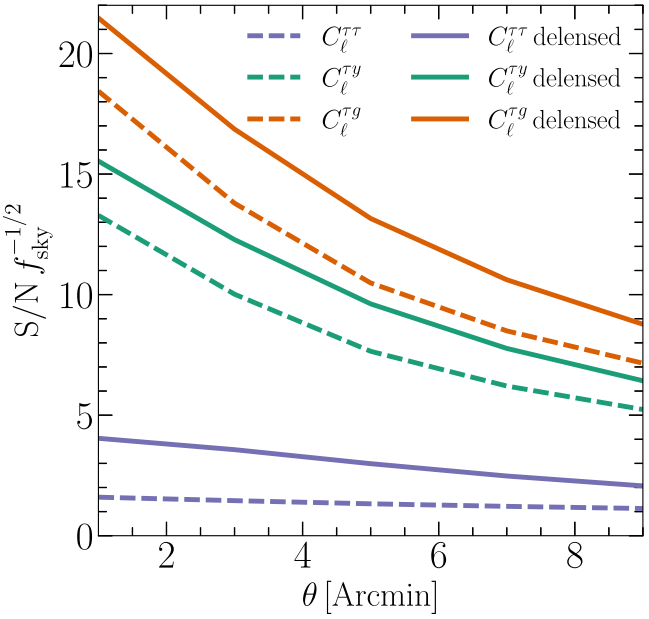

Figure 2. Forecast of S/N of $C_\ell^{\tau g}$, $C_\ell^{\tau y}$, and $C_\ell^{\tau\tau}$ signals with FWHM of the beam for the CMB-S4-like experiment for $M_{\rm min} = 2 \times 10^{11}\, M_\odot$ and $M_{\rm max} = 10^{13}\, M_\odot$. The cross-correlations are calculated using the analytic halo model and the instrumental sensitivity in temperature is set to 1 μK arcmin. The S/N increases with the smaller beam size because the number of accessible modes increases with the resolutions of an experiment. In addition to that, the delensing of B modes helps to reduce the noise in polarizations that lower the reconstruction noise of τ fluctuations.

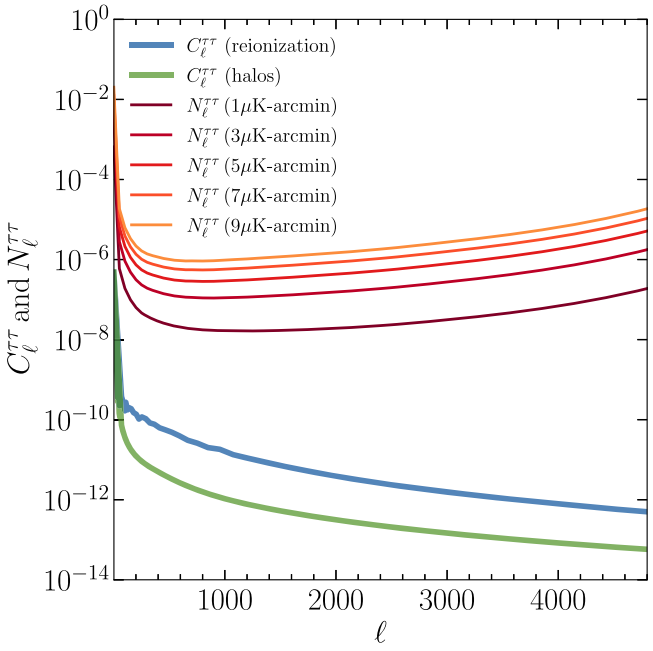

Figure 3. Reconstruction noise of optical depth power spectrum corresponding to different sensitivities in temperature of a CMB experiment, while the FWHM of the beam is fixed at 1′. $C_\ell^{\tau\tau}$ from reionization and halos ($M > 3 \times 10^{13}\, M_\odot$) are calculated from hydrodynamic simulations (Battaglia et al. 2012).

In the nonrelativistic limit, the tSZ spectral dependence is very well defined, and it helps to minimize the variance to reconstruct the signal from the total observed signal. Since we are interested in measuring the yy autopower spectrum in the absence of the cosmic infrared background (CIB; generally the largest contaminant to tSZ observations), we can write down a model for an angular scale (d) per frequency (ν) as (Planck Collaboration et al. 2016)

$$d_{\ell,\nu} = a_{\ell,\nu} f_\nu^y\, C_\ell^y + b_{\ell,\nu} f_\nu^{\rm CIB}\, C_\ell^{\rm CIB} + n_{\ell,\nu}, \tag{27}$$

where a and b are the scale- and frequency-dependent coefficients. We will refer to n as noise, but it also contains primordial CMB fluctuations, radio sources, instrumental noise, etc. The cILC algorithm constructs a weight vector W such that we get a unit response to a (the tSZ coefficients) and a null response to b (the CIB coefficients), $W^T \boldsymbol{a} = 1\; W^T \boldsymbol{b} = 0$. The general solution for W was shown in Remazeilles et al. (2011),

$$W_{a=1,b=0} = \frac{b^T n^{-1} b a^T n^{-1} - a^T n^{-1} b b^T n^{-1}}{a^T n^{-1} a b^T n^{-1} b - (a^T n^{-1} b)^2}. \tag{28}$$

Note that we dropped the frequency dependence for clarity. From the weight we can calculate N_ℓ^{yy} via

$$N_\ell^{yy} = \sum_\nu (W_\nu n_\nu W_\nu^T)_\ell. \tag{29}$$

We use the SILC[8] package to estimate N_ℓ^{yy} in the presence of primordial CMB and cosmic infrared background and foreground due to the dust and synchrotron radiation. In the near future, low-noise experiments will be able to produce signal-dominated measurements of the tSZ effect (Hanany et al. 2019).

4.3. Shot Noise of Galaxy Power Spectrum

For the case of the noise power spectrum of galaxies, we assume that the process of local galaxy formation in halos is linear and that the dominant source of noise is the shot noise term for the measurement of galaxy power spectra. In this regime, the shot noise becomes equal to $1/\bar{n}_{\rm g}$, where $\bar{n}_{\rm g}$ is the average number density of galaxies. The average number density of galaxies at z can be written as

$$\bar{n}_g(z) = \int_{M_{\rm min}}^{M_{\rm max}} dM \frac{dn(M, z)}{dM} N_g(M, z). \tag{30}$$

We consider the specifications of the VRO[9] to determine the shot noise term. We fix $M_{\rm max} = 10^{13}\, M_\odot$ and consider a redshift distribution of galaxies in the redshift range $z_{\rm min} = 0$ and $z_{\rm max} = 5$ as described in Abell et al. (2009). The total number of galaxies that will be probed by a VRO-like experiment is 50 per square arcminute. Using Equation (30), we find $M_{\rm min} = 2 \times 10^{11}\, M_\odot$ satisfies this condition and we use this value of $M_{\rm min}$ for making forecasts for a VRO-like experiment.

5. Detectability of Signals

In this section, we discuss the detectability of the cross-correlation between different observational probes that are described in Section 2. For the forecasts, we used the sensitivity of the CMB-S4-like experiment with the sensitivity, $\Delta_T = 1\; \mu K$ arcmin, and the FWHM of the beam, $\theta_{\rm f} = 1'$.

As discussed in the previous section, we assume that the estimator described in Dvorkin & Smith (2009) can reconstruct

[8] https://github.com/nbatta/SILC

[9] https://www.lsst.org/

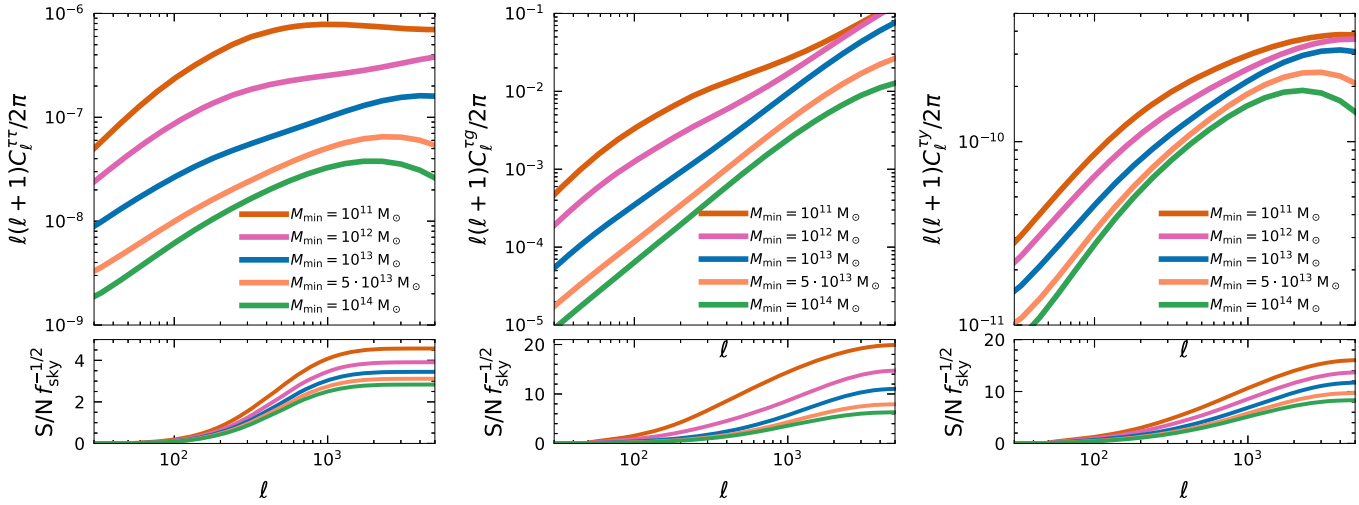

Figure 4. Top panel: $\tau\tau$ (left panel), τg (middle panel), and τy (right panel) power spectra shown as a function of the minimum halo mass, $M_{\rm min}$. Bottom panel: cumulative S/Ns calculated for the $\tau\tau$ (left panel), τy (middle panel), and τg (right panel) with 1 μK arcmin sensitivities in temperature and $1'$ beam size. This figure shows that S/Ns are dominated by the low-mass halos ($M_{\rm halo} \lesssim 10^{12}\,M_\odot$) rather than the high-mass halos ($M_{\rm halo} \gtrsim 10^{13}\,M_\odot$).

Table 3
The Forecasted 1σ Uncertainties on the Parameters of Density and Pressure Profiles

Parameters	Meaning	Fiducial Values	$\tau g + gg$	$\tau y + yg + gg$	$yg + gg$	Joint Analysis
A_{ρ_0}	Amplitude of density profile	4000	7.27	13.2	⋯	6.38
A_{P_0}	Amplitude of pressure profile	18.1	⋯	13.64	14.32	13.65
$A_{\rm xc}$	Amplitude of characteristic scale of halo	0.497	⋯	12.9	13.54	12.86
$A_{\beta p}$	Power-law index of the fall of pressure profile	4.35	⋯	6.0	6.35	6.0

a fluctuating τ map, and this map is then cross-correlated with a given galaxy sample or with a Compton y map, which produces cross spectra ($C_\ell^{\tau g}$ and $C_\ell^{\tau y}$, respectively). A similar approach was proposed to measure the fluctuations in τ from reionization by cross-correlating with measurements from 21 cm experiments (Meerburg et al. 2013; Roy et al. 2020).

The total S/N is calculated by summing the signal-to-noise per ℓ mode,

$$({\rm S/N})^2 = \sum_\ell \left(\frac{C_\ell^{XY}}{\Delta C_\ell^{XY}}\right)^2, \tag{31}$$

where ΔC_ℓ^{XY} is a theoretical error on C_ℓ^{XY} given $N_\ell^{\tau\tau}$. The exact form of ΔC_ℓ^{XY} we use is

$$(\Delta C_\ell^{XY})^2 = \frac{1}{(2\ell+1) f_{\rm sky}^{XY}}[(C_\ell^{XY})^2 + (C_\ell^{XX} + N_\ell^{XX})(C_\ell^{YY} + N_\ell^{YY})], \tag{32}$$

where $f_{\rm sky}^{XY}$ is the fraction of sky covered and C_ℓ^{XX} and N_ℓ^{YY} are the autospectrum and noise term of a given tracer, respectively. Here we assume that $N_\ell^{\tau\tau} \gg C_\ell^{\tau\tau}$ to simplify Equation (32).

We use the simulations described in Section 3 to calculate the cross-power spectra $C_\ell^{\tau g}$ and $C_\ell^{\tau y}$. Here the field g refers to a number-count map where a nonzero value is assigned at the location of each halo above a given minimum mass, and y is a Compton y map with the same mass threshold. We cross-correlate the number-count and Compton y maps with the simulated τ maps. Then, for each redshift, we average over all simulation realizations and add these differential cross-spectra to obtain the signal.

Note that all of the cross-correlations have contributions both from the high redshift ($z \gtrsim 5$) and low redshift ($z \lesssim 5$). The yy from reionization is subdominant as the power spectrum is at least 3–4 orders of magnitude smaller than the galaxy and cluster contributions (Hill et al. 2015), but the amplitude of the τy power spectrum from reionization is comparable with the contributions from halos at low redshift (though they may have different shapes as the characteristic scale of ionized bubbles and halos are different; Hill et al. 2015; Namikawa et al. 2021). We calculate the τy signal for a fiducial model of reionization with the characteristic bubble size of ionized bubbles $\bar{R}_b = 5$ Mpc following a semianalytic model described in Namikawa et al. (2021). Hence, we consider the τy signal from reionization as a source of noise in our forecasts. yg and τg from high and low redshift do not correlate as we choose the galaxy distribution function at the low redshift only, so they have different kernels.

In Figure 2, we show the total S/N as a function of beam size for the CMB-S4-like survey that has a noise level of 1 μK arcmin. The ℓ range we consider is from 100 to 5000 in polarization. For a halo mass threshold of $M_{\rm min} = 2 \times 10^{11} M_\odot$ and $\theta_{\rm fwhm} = 1'$, we find the total ${\rm S/N} f_{\rm sky}^{-1/2} \approx 15$ and 10 for $C_\ell^{\tau g}$ and $C_\ell^{\tau y}$, respectively. After delensing the lensed B-mode power spectrum at the level of 90% (Smith et al. 2012; Abazajian et al. 2019), we find that the S/N increases by 14% and 12.5% for $C_\ell^{\tau g}$ and $C_\ell^{\tau y}$, respectively.

In Figure 4, we show the variation of τy, τg, and τy signals for different minimum halo masses, $M_{\rm min}$. The cumulative

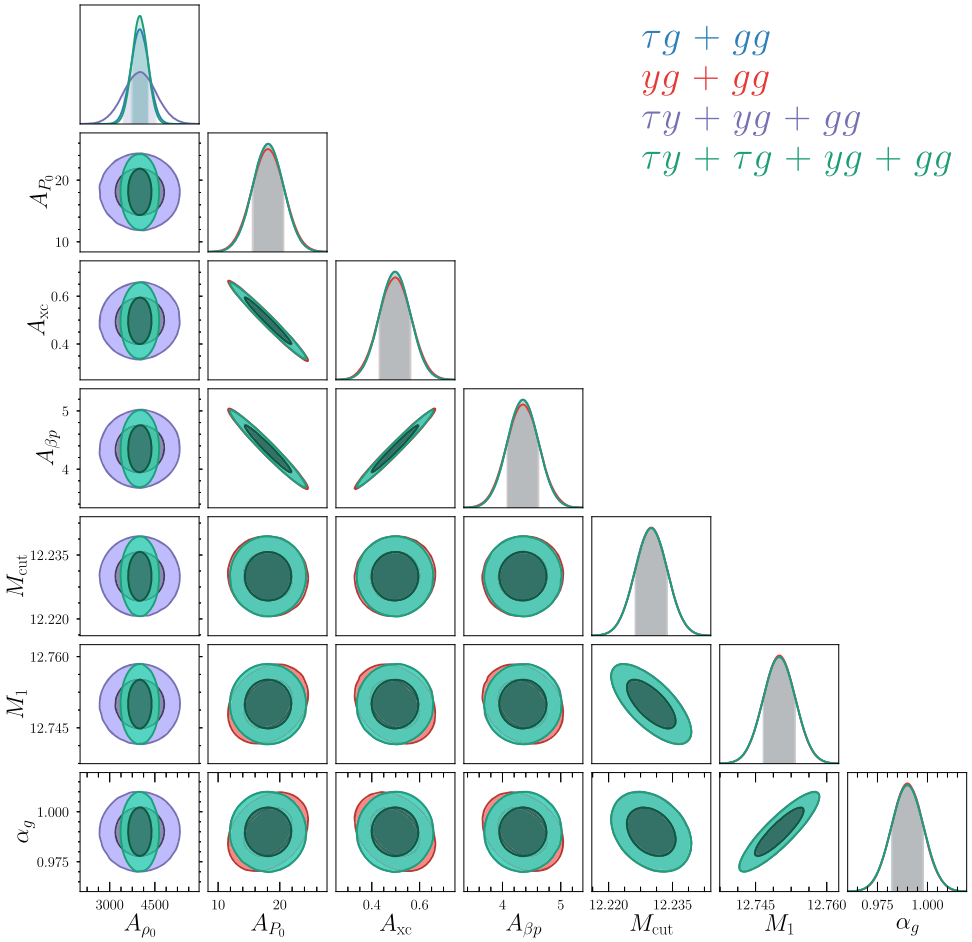

Figure 5. Forecasted constraints on the density, pressure, and HOD parameters from the different combinations of τg, τy, and yg. We set $M_{\rm min} = 2 \times 10^{11}\,M_\odot$ and $M_{\rm max} = 10^{13} M_\odot$ to study the properties of the CGM. Tight constraints are placed on HOD parameters from the measurements of C_ℓ^{gg}.

S/Ns for τg, τy, and $\tau\tau$ are 20, 16, and 5.5 corresponding to $M_{\rm min} = 10^{11}\,M_\odot$. The S/Ns change to 11, 11.5, and 4 if $M_{\rm min}$ is set to $10^{13}\,M_\odot$. We find the S/N for yg is 1710 and 950 for $M_{\rm min} = 10^{11}\,M_\odot$ and $10^{14}\,M_\odot$, respectively.

6. Fisher Forecast

In this section, we discuss how the future measurements of these cross-correlations can be used to constrain the astrophysical parameters related to the pressure and density of the CGM. For the rest of our analysis, we use the upper limit on the halo mass of $M_{\rm max} = 10^{13}\,M_\odot$ so that we can study the properties of the CGM. We assume that the pressure and density profile is self-similar to the redshift and mass of halos.

We use a Fisher matrix analysis to forecast the measurement uncertainties of the parameters of our interest. The Fisher matrix is given by

$$F_{ij} = \sum_\ell \frac{1}{(\Delta C_\ell^{XY})^2} \frac{\partial C_\ell^{XY}}{\partial P_i} \frac{\partial C_\ell^{XY}}{\partial P_j}, \tag{33}$$

where P_i and P_j are the parameters that we aim to constrain from the measurements of cross-correlations.

We select parameters of pressure and density, as described in Table 3, and show the constraints on parameters in Figure 5 for the different combinations of the τg, yg, τy, and gg signals. Note that the yg signal can probe the parameters related to the pressure profile, whereas the τg signal is sensitive to the density profile of halos. The τy signal is sensitive to both the pressure and density profile, and for this reason, we use it to break the degeneracy between the amplitude of density and pressure profiles. We use $M_{\rm min} = 2 \times 10^{11}\,M_\odot$, $z_{\rm max} = 5$, and $f_{\rm sky} = 0.5$ for this analysis. The galaxy power spectrum puts tighter constraints on the HOD model than the parameters that are inferred from the yg signal and it helps to break the degeneracy between parameters of pressure and the HOD model. We present our forecasts of the parameters in Table 3.

The detection of these cross-correlations leads us to understand some other astrophysical parameters that are directly related to the pressure and density profiles. We specifically focus on the gas mass fraction, $f_{\rm g} = M_{\rm gas}/M_{\rm halo}$. It should be noted that this quantity depends on the definition of the radius and mass of halos. For example, the value of $f_{\rm g}$ will be different for the radii R_{200}, R_{500}, and R_{2500} as they correspond to different halo masses M_{200}, M_{500}, and M_{2500}.

The $M_{\rm gas}$ inside R_{500} can be written as

$$M_{\rm gas,500}(z) = \int_0^{R_{500}} \rho_{\rm gas}(r, z)\, 4\pi r^2 dr. \tag{34}$$

In Figure 6, we show the forecasted constraints on the amplitude of the density profile A_ρ from the τg and τy signals. As expected, τg put tighter limits on the A_ρ as the S/N is larger

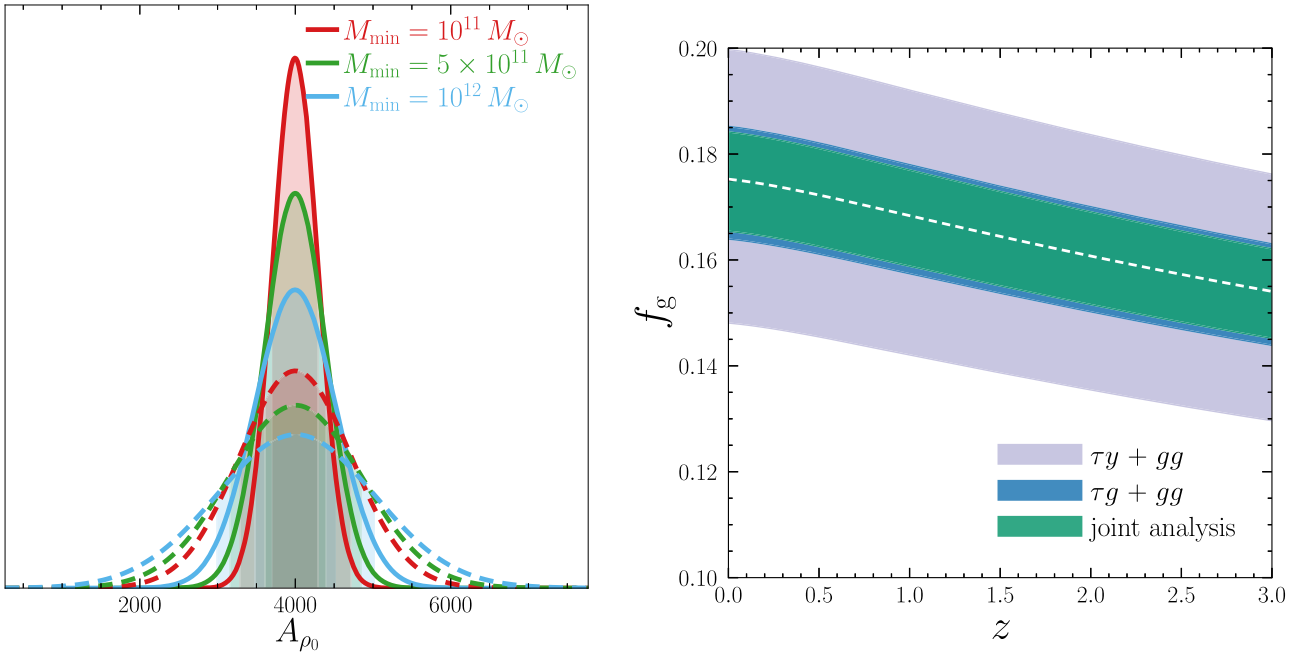

Figure 6. Left: the solid lines show the constraints on the amplitude of the density profile, A_ρ, from τg cross-correlations, and the dashed lines represent the constraints inferred from τy cross-correlation. Right: the forecasted 1σ uncertainty of the gas mass fraction, $f_{\rm g}$, calculated from a joint analysis of different probes of cross-correlation. The dashed white line is the best-fit curve for the $\tau y + \tau g + yg + gg$.

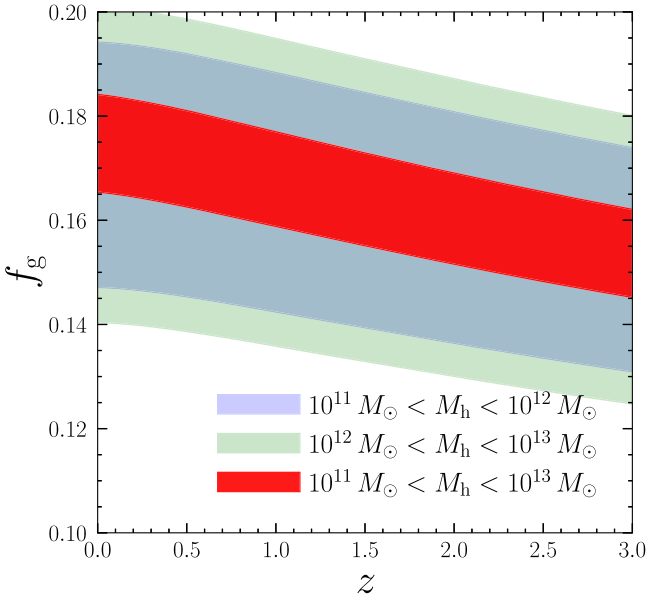

Figure 7. We show the forecasted uncertainties (1σ) on the measurements of $f_{\rm g}$ for three different choices of $M_{\rm min}$ and $M_{\rm max}$.

than the τy for the same $M_{\rm min}$. We find that the gas mass fraction, $f_{\rm g}$, can be measured with more than 7σ confidence for $\tau y + gg$ and 17σ for $\tau g + gg$. The gas mass fraction is a model-dependent quantity, as we assume a particular density and pressure profile and the definition of mass and radius of a halo. In Figure 7, we show the combined constraints on $f_{\rm g}$ for the choice of different mass bins. The measurement uncertainty on $f_{\rm g}$ increases approximately by 25% for the mass bin $[10^{11}, 10^{12}]$ than the mass bin $[10^{12}, 10^{13}]$. This is because there are more halos for the lower mass bin that correlate with the fluctuations in optical depth; hence, the S/N increases significantly.

7. Discussion

In the near future, there will be signal-dominated high-resolution tSZ measurements that will bring a unique opportunity to break the degeneracy among astrophysical parameters related to the thermodynamic properties of the CGM by performing cross-correlation with other probes. We explored such cross-correlations to measure the density and pressure profiles of halos using independent observational probes. In this paper, we presented the detectability of cross-correlations between the optical depth anisotropy (reconstructed from the CMB polarization anisotropy), Compton y parameter (derived from the CMB temperature measurements), and galaxy overdensity field. The optical depth anisotropy is a tracer of the gas density distribution in halos, the Compton y parameter probes the pressure profile, and the galaxy number count carries information on the distribution of galaxies in dark matter halos.

We used a semianalytic halo-model formalism (compared against hydrodynamic simulations) to estimate the power spectra of these cross-correlated signals. The yg signal is the most promising probe for constraining the pressure parameters, which can be performed using VRO galaxies and the Compton y map from the CMB-S4 experiment. We estimate the cross-correlated signals using cosmological simulations and compared the results with halo-model formalism for the mass of the halos, $M_{\rm h} > 10^{13}\,M_\odot$. We find the S/N can reach as high as 500–2000 depending on the $M_{\rm min}$. Such a high S/N can be used to understand the subgrid physics in halos, such as AGN feedback, turbulence, and the depletion efficiency of gas in the CGM.

The thermodynamic properties of the CGM are very complex and the modeling of different physical processes is a challenging job. There are varieties of simulations based on galaxy formation models that probe the CGM properties. In this paper, we use cosmological simulations based on a parametric model of pressure and density profiles, as the detailed comparison of constraints on the CGM profile is out of the

scope of this paper. Moreover, it is broadly found that the pressure and density profiles of the CGM calculated from different simulations do not match the observed CGM profile (Amodeo et al. 2021; Moser et al. 2022). The choice of simulations to probe the detailed physics of the CGM could be helpful if the S/Ns were significantly high. In our case, we forecasted the constraints on f_g based on halo-model formalism for a moderate value of S/N.

On the other hand, the τg signal is a useful probe for measuring the density profile along with the priors on HOD model parameters that can be well achieved by the precise measurement of the gg signal alone. The measurements of pressure and density profiles by different probes, such as τg, yg, and yg, will also lead us to determine the temperature profile of halos. A joint analysis will not only improve our understanding of the low-redshift universe but will also help us to investigate the reionization process. The $y\tau$ signal at low redshift contaminates the $y\tau$ signal from reionization. Hence, a proper estimation of $y\tau$ from halos will help to remove it from the total observed signal, which can put tighter constraints on reionization parameters such as the size and temperature of ionized bubbles (Namikawa et al. 2021).

The multiple probes presented in this paper are complementary to tSZ and kSZ measurements and their cross-correlations with galaxy surveys. Previous kSZ measurements have probed the average density profile of halos (Schaan et al. 2016; Amodeo et al. 2021; Schaan et al. 2021). However, spectroscopic galaxy redshifts are required to reconstruct the velocity field to achieve these constraints on the density profile. The cross-correlations we propose do not require spectroscopic information of galaxies. Instead, we forecast complementary and comparable constraints by utilizing a larger sample of galaxies selected from future imaging surveys. Our forecasts show that the cross-correlation between τ and g is detectable with more than 15 σ for upcoming experiments, whereas the autopower spectrum of τ is detectable at $\sim 4\sigma$.

Baryons that are outside the halos are hard to see in optical and X-ray bands, but their presence is encoded in the optical depth anisotropies as these baryons interact with CMB photons via Thomson scattering. The cross-correlations presented here are sensitive to the global properties of gas inside and outside halos. Thus, probing the baryon abundances inside and outside halos with such cross-correlations can be used to resolve the question of are we missing baryons? Furthermore, we demonstrated that our proposed joint cross-correlations are robust. We found that "bias hardening" the estimator to reduce leakage from CMB lensing did not have an appreciable impact on the results.

Acknowledgments

The authors would like to thank Stefania Amodeo, Joel Meyers, Connor Sheere, Kendrick Smith, and David Spergel. V.G. is supported by the National Science Foundation under grant No. PHY-2013951. N.B. acknowledges support from NSF grant AST-1910021 and NASA grants 21-ADAP21-0114 and 21-ATP21-0129.

ORCID iDs

Anirban Roy https://orcid.org/0000-0001-5729-0246

References

Abazajian, K., Addison, G., Adshead, P., et al. 2019, arXiv:1907.04473
Abell, P. A., Allison, J., Anderson, S. F., et al. 2009, arXiv:0912.0201
Ade, P., Aguirre, J., Ahmed, Z., et al. 2019, JCAP, 2019, 056
Aghanim, N., Akrami, Y., Ashdown, M., et al. 2018, A&A, 617, A48
Aiola, S., Calabrese, E., Maurin, L., et al. 2020, JCAP, 2020, 047
Alonso, D., Louis, T., Bull, P., & Ferreira, P. G. 2016, PhRvD, 94, 043522
Amodeo, S., Battaglia, N., Schaan, E., et al. 2021, PhRvD, 103, 063514
Battaglia, N. 2016, JCAP, 2016, 058
Battaglia, N., Bond, J. R., Pfrommer, C., & Sievers, J. L. 2012, ApJ, 758, 75
Battaglia, N., Bond, J. R., Pfrommer, C., Sievers, J. L., & Sijacki, D. 2010, ApJ, 725, 91
Battaglia, N., Hill, J. C., & Murray, N. 2015, ApJ, 812, 154
Calafut, V., Gallardo, P. A., Vavagiakis, E. M., et al. 2021, PhRvD, 104, 043502
Chluba, J., Nagai, D., Sazonov, S., & Nelson, K. 2012, MNRAS, 426, 510
Cooray, A., & Sheth, R. K. 2002, PhR, 372, 1
De Bernardis, F., Aiola, S., Vavagiakis, E. M., et al. 2017, JCAP, 2017, 008
Dvorkin, C., Hu, W., & Smith, K. M. 2009, PhRvD, 79, 107302
Dvorkin, C., & Smith, K. M. 2009, PhRvD, 79, 043003
Enßlin, T. A., Pfrommer, C., Springel, V., & Jubelgas, M. 2007, A&A, 473, 41
Eriksen, H. K., Banday, A. J., Gorski, K. M., & Lilje, P. B. 2004, ApJ, 612, 633
Feng, C., & Holder, G. 2018, PhRvD, 97, 123523
Feng, C., & Holder, G. 2019, PhRvD, 99, 123502
Ferraro, S., Hill, J. C., Battaglia, N., Liu, J., & Spergel, D. N. 2016, PhRvD, 94, 123526
Gluscevic, V., Kamionkowski, M., & Hanson, D. 2013, PhRvD, 87, 047303
Greco, J. P., Hill, J. C., Spergel, D. N., & Battaglia, N. 2015, ApJ, 808, 151
Guzman, E., & Meyers, J. 2021, PhRvD, 104, 043529
Hanany, S., Alvarez, M., Artis, E., et al. 2019, arXiv:1902.10541
Hill, J. C., Battaglia, N., Chluba, J., et al. 2015, PhRvL, 115, 261301
Hill, J. C., Ferraro, S., Battaglia, N., Liu, J., & Spergel, D. N. 2016, PhRvL, 117, 051301
Hill, J. C., & Pajer, E. 2013, PhRvD, 88, 063526
Hill, J. C., & Spergel, D. N. 2014, JCAP, 2014, 030
Hojjati, A., Tröster, T., Harnois-Déraps, J., et al. 2017, MNRAS, 471, 1565
Hurier, G., Douspis, M., Aghanim, N., et al. 2015, A&A, 576, A90
Jubelgas, M., Springel, V., Enßlin, T., & Pfrommer, C. 2008, A&A, 481, 33
Knox, L. 1995, PhRvD, 52, 4307
Komatsu, E., & Kitayama, T. 1999, ApJL, 526, L1
Koukoufilippas, N., Alonso, D., Bilicki, M., & Peacock, J. A. 2020, MNRAS, 491, 5464
Kusiak, A., Bolliet, B., Ferraro, S., Hill, J. C., & Krolewski, A. 2021, PhRvD, 104, 043518
Lewis, A., Challinor, A., & Lasenby, A. 2000, ApJ, 538, 473
Madhavacheril, M. S., Battaglia, N., Smith, K. M., & Sievers, J. L. 2019, PhRvD, 100, 103532
Meerburg, P. D., Dvorkin, C., & Spergel, D. N. 2013, ApJ, 779, 124
Meinke, J., Böckmann, K., Cohen, S., et al. 2021, ApJ, 913, 88
Moser, E., Amodeo, S., Battaglia, N., et al. 2021, ApJ, 919, 2
Moser, E., Battaglia, N., Nagai, D., et al. 2022, ApJ, 933, 133
Namikawa, T. 2018, PhRvD, 97, 063505
Namikawa, T., Hanson, D., & Takahashi, R. 2013, MNRAS, 431, 609
Namikawa, T., Roy, A., Sherwin, B. D., Battaglia, N., & Spergel, D. N. 2021, PhRvD, 104, 063514
Navarro, J. F., Frenk, C. S., & White, S. D. M. 1996, ApJ, 462, 563
Nielsen, N. M., Churchill, C. W., Kacprzak, G. G., Murphy, M. T., & Evans, J. L. 2015, ApJ, 812, 83
Nozawa, S., Itoh, N., Suda, Y., & Ohhata, Y. 2006, NCimB, 121, 487
Pandey, S., Baxter, E. J., & Hill, J. C. 2020, PhRvD, 101, 043525
Pandey, S., Gatti, M., Baxter, E., et al. 2022, PhRvD, 105, 123526
Pfrommer, C., Springel, V., Enßlin, T. A., & Jubelgas, M. 2006, MNRAS, 367, 113
Planck Collaboration, Ade, P. A. R., Aghanim, N., et al. 2016, A&A, 594, A25
Planck Collaboration, Aghanim, N., Akrami, Y., et al. 2020, A&A, 641, A6
Reichardt, C. L., Patil, S., Ade, P. A. R., et al. 2021, ApJ, 908, 199
Remazeilles, M., Delabrouille, J., & Cardoso, J.-F. 2011, MNRAS, 410, 2481
Roy, A., Kulkarni, G., Meerburg, P. D., et al. 2021, JCAP, 2021, 003
Roy, A., Lapi, A., Spergel, D., & Baccigalupi, C. 2018, JCAP, 2018, 014
Roy, A., Lapi, A., Spergel, D., Basak, S., & Baccigalupi, C. 2020, JCAP, 2020, 062
Schaan, E., Ferraro, S., Vargas-Magaña, M., et al. 2016, PhRvD, 93, 082002
Schaan, E., Ferraro, S., Amodeo, S., et al. 2021, PhRvD, 103, 063513
Scoccimarro, R., Sheth, R. K., Hui, L., & Jain, B. 2001, ApJ, 546, 20
Shao, J., & Fang, T. 2016, MNRAS, 458, 3773

Singh, P., Majumdar, S., Nath, B. B., Refregier, A., & Silk, J. 2016, MNRAS, 456, 1495
Smith, K. M., Hanson, D., LoVerde, M., Hirata, C. M., & Zahn, O. 2012, JCAP, 2012, 014
Sobrin, J. A., Anderson, A. J., Bender, A. N., et al. 2022, ApJS, 258, 42
Springel, V. 2005, MNRAS, 364, 1105
Springel, V., & Hernquist, L. 2003, MNRAS, 339, 289
Su, M., Yadav, A. P. S., McQuinn, M., Yoo, J., & Zaldarriaga, M. 2011, arXiv: 1106.4313
Sunyaev, R. A., & Zeldovich, Y. B. 1970, Ap&SS, 7, 3
Sunyaev, R. A., & Zeldovich, Y. B. 1972, CoASP, 4, 173
Tinker, J. L., Kravtsov, A. V., Klypin, A., et al. 2008, ApJ, 688, 709
Tumlinson, J., Peeples, M. S., & Werk, J. K. 2017, ARA&A, 55, 389
Vavagiakis, E. M., Gallardo, P. A., Calafut, V., et al. 2021, PhRvD, 104, 043503
Werk, J. K., Prochaska, J. X., Tumlinson, J., et al. 2014, ApJ, 792, 8
Yan, Z., van Waerbeke, L., Tröster, T., et al. 2021, A&A, 651, A76
Zhao, H. 1996, MNRAS, 278, 488
Zheng, Z., Berlind, A. A., Weinberg, D. H., et al. 2005, ApJ, 633, 791